Thermocapillary convection in a laser-heated Ni melt pool: A molecular dynamics study

O. Politano, Florence Baras

Thermocapillary convection in a laser-heated Ni melt pool: a molecular dynamics study

O. Politano* and F. Baras†

Laboratoire ICB UMR 6303 CNRS-Université de Bourgogne,

9 Avenue A. Savary, BP 47870, 21078 Dijon Cedex, France.

(Dated: September 7, 2023)

Abstract

Thermocapillary convection was investigated in a metallic system of pure Ni, at the nanoscale, by molecular dynamics. The system interface was irradiated by a heat flux, mimicking a focused laser source. The melt pool was submitted to a large temperature gradient that modified the surface tension along the interface. In liquid metal, because surface tension typically decreases with increasing temperature, the result is a gradient of surface tension along the free surface. The liquid metal, therefore, started to flow in the direction of high surface tension. Two counter-rotating convection cells developed, characteristic of those observed in welding and other material processing. A systematic estimation of relevant parameters in hydrodynamics allowed us to interpret the results in terms of Prandtl, Marangoni, and Péclet numbers. This study demonstrates the influence of laser power and system size on pool shape and flow characteristics.

Cite as: J. Appl. Phys. 134, 095301 (2023);

doi: 10.1063/5.0167061

Submitted: 10 July 2023. Accepted: 14 August 2023

* Olivier.Politano@u-bourgogne.fr

† Florence.Baras@u-bourgogne.fr

I. INTRODUCTION

Thermocapillary convection is a ubiquitous phenomenon in various processes used in Materials Science, e.g. welding [1], growth of crystals in semiconductor materials [2], rupture of thin films in heat transfer devices [3], texturing of surfaces in magnetic storage devices [4], selective laser melting [5], epitaxial laser metal forming [6], assembly of liquid metal filaments [7], and laser surface hardening [8]. Although much studied, this phenomenon still attracts considerable attention because of the wide range of applications affected by it.

A temperature gradient applied on a free-surface fluid results in a surface tension gradient. In order to balance the surface tension gradient, shear stresses arise at the interface and induce a fluid motion. This is known as the Marangoni effect. In 1900, Bénard first observed cellular flow patterns in a fluid heated from below [9]. This observation was attributed to buoyancy until Pearson's famous paper published in 1958 [10]. Pearson realized that cellular patterns can also appear in drying thin paint films, where gravity is reversed in comparison to Bénard experiments. He was the first to provide the correct explanation in terms of the Marangoni effect: the surface tension forces are sufficient to cause instability and are responsible for cellular patterns in cooling fluid layers with at least one free surface. In small geometry and/or microgravity environments, thermocapillarity is dominant over buoyancy. There are two typical situations [11]: when the temperature gradient is perpendicular to the interface, Marangoni convection instability occurs if the gradient exceeds a critical threshold. When the temperature gradient is parallel to the interface, thermocapillary convection occurs for any value of the temperature gradient. Both types exist in Materials Science processes. Typically, the rupture of thin films in heat transfer devices [3] corresponds to Marangoni convection. Thermocapillary convection has been studied for specific geometries in which a liquid is confined between solid plates maintained at different temperatures. They are classified as a function of the direction of gravity $\vec{g}$, with respect to the temperature gradient $\vec{\nabla}T$: the liquid bridge ($\vec{g} \parallel \vec{\nabla}T$), the rectangular layer ($\vec{g} \perp \vec{\nabla}T$), and the annular geometry.

The liquid bridge (also called half-zone) was considered a candidate for manufacturing semiconductor materials in micro-gravity platforms. Crystals grown in such conditions [12] show dopant striations caused by oscillatory thermocapillary convection, rather than buoyancy-driven convection.

In most situations of practical interest in Material Sciences, the heat source is a laser that melts a powder bed or solid surface. The hydrodynamics of a melt pool, induced by laser heating during welding, has been investigated since the 1980s. Experimentally, the flow is difficult to observe in a metallic weld pool due to its opacity. In order to visualize the flow, Limmaneevichitr and Kou used a transparent pool of $NaNO_3$ with a Marangoni number close to that of metals used in welding experiments [13]. They suggested that Marangoni convection dominates over gravity-induced convection. Undoubtedly, fluid motion in pure liquid metals is induced by temperature-dependent surface tension at the free surface of the melt pool. The surface tension, γ, between the liquid and the surrounding gas reads

$$\gamma(T) = \gamma_m + \gamma_T (T - T_m) \tag{1}$$

where T_m is the melting temperature, $\gamma_m = \gamma(T_m)$, and $\gamma_T < 0$ where $\gamma_T \equiv -d\gamma/dT > 0$ is the surface tension gradient. The largest values of γ typically occur at the coldest regions of the interface. Thus, the surface flow tends to go from hot to cold regions. Adding a surface-active agent in the liquid metal (for example, sulfur in stainless steel) leads to a change of γ_T from negative to positive values. As a consequence, the flow pattern is reversed and the weld penetration increases [1].

Laser surface treatment is characterized by very localized heat input, leading to large radial temperature gradients at the melt pool surface. Heat input depends on laser power and beam diameter. Modeling melt pool convection mainly relies on a multiphysics description. The governing equations of the transport processes in the melt pool include momentum and energy conservation equations. The laser input heat flux is usually described by a Gaussian energy distribution [5]. The Marangoni effect is modeled as a shear stress on the upper surface of the melt pool. The side and bottom surfaces are

set at a fixed temperature. Boundary conditions at the melt surface include laser beam deposition, force convection, heat dissipation, and heat radiation [14]. This complete set of equations is solved numerically with finite element methods in order to simulate temperature distribution, flow activity, and melt pool shape. In the present work, we studied the hydrodynamic behavior of a Ni melt pool, created by laser heating, by means of molecular dynamics (MD) simulations. This approach questions the very existence of thermocapillary convection at nanoscale. This method presents the advantage of focusing only on purely thermal effects that could be responsible for the onset of thermocapillary convection. As in micro-gravity experiments, buoyancy effects are dismissed. In addition, MD simulations allow direct visualization of metallic flows.

The emergence of collective behavior in systems composed of a few thousands of particles attracted attention in the late 1980s. Mareschal and Kestemont reported the observation of Bénard convection in a system of 5000 hard disks, in the presence of both a thermal gradient and an external constant force [15]. These results were in agreement with classical hydrodynamics, in which transport coefficients are those of hard-disk Enskog gas [16]. Following this pioneering work, a large variety of complex hydrodynamic flows have been investigated in microscopic simulations: e.g. the Pouiseuille flow [17], and the Rayleigh-Taylor instability [18]. The use of atomistic techniques captures physical effects not resolved by more traditional continuum methods [19]. The critical role of thermal fluctuations at nanoscale has been demonstrated in the case of the Rayleigh-Plateau instability [20].

In systems with an interface, surface tension variation plays the role of driving force for interfacial flows. The fluid is dragged along the interface in the direction of lower surface tension. Variations in surface tension are due to temperature gradient (eq. (1)), concentration gradient, or electric charge. Solutal Marangoni convection, which is associated with concentration gradient, has been studied in MD simulations of a nanometric thin liquid film composed of solute, water, and argon, and MD observations were compared to computational fluid dynamics simulations [21]. Observation of thermocapillary

convection has been reported in NEMD (non-equilibrium) simulations in which a model liquid biphasic mixture is confined between thermalized regions [22].

Fluid dynamics at nanoscale is particularly important in several applications. Capillary and Marangoni flows play a key role in thermal management devices such as heat-pipes [23, 24]. Another application is the nanometric flow of molten polyethylene induced by a heated atomic force microscope (AFM) tip during nanolithography [25]. The polymer flow was found to be governed by thermal Marangoni forces and non-equilibrium wetting dynamics. Nanometric-scale manufacturing with focused ion beams is also developing fast for applications such as forming nanopores in thin films for DNA sequencing. Atomic-scale thermocapillary flow was demonstrated in this process by means of MD simulations [26].

The specific model designed to study the flow dynamics in a nanometric metallic system is introduced in Sec. II, which also includes a synopsis of the simulation procedure. In Sec. III, we analyze the results and show the flow developed in the presence of a temperature gradient at the interface. Section III A summarizes the thermodynamic and physical properties of liquid nickel. More specifically, we give the results of simulations designed specifically to obtain the temperature dependence of surface tension and viscosity. In this section, we introduce the main non-dimensional parameters that are relevant in the description of hydrodynamics in this system. In Sec. III B, we present the characteristics of a melt pool flow, along with melt pool shape. We discuss the influence of laser intensity and system size. Finally, the main conclusions are presented in Sec.IV.

II. METHODS

Melt pool dynamics is investigated using million-atom molecular dynamics (MD) in a quasi- two-dimensional cell (or pseudo 3D geometry). The typical box size is L_x=249.5 nm, L_y=1.426 nm and L_z=139 nm (number of atoms $\sim 2.6 \times 10^6$). Atomic

trajectories were integrated by a velocity-verlet integrator with LAMMPS [27] using the Embedded Atom Potential (EAM) formulated by Purja and Mishin for the Ni-Al system [28]. This potential is known to reproduce well the physical and thermodynamic properties of nickel [29]. The time step was fixed at 1 fs. Periodic boundaries were applied along all three directions, and a vacuum of 57 nm was inserted above the nickel slab (see Fig. 1).

Note that the nickel system was created at 1300 K using an appropriate lattice parameter (i.e., linear expansion for the potential was computed in Ref. [29]). Then the whole system was shortly relaxed during 20 ps in the NPT ensemble, using a Nose-Hoover thermostat and barostat with temperature and pressure damping parameters equal to 0.1 and 1.0 ps. After that preliminary stage, atoms located at the borders (i.e. $x < 10.7$ nm, $x > L_x - 10.7$ nm and $z < 10.7$ nm) were kept at 1300 K with a Langevin thermostat, whereas other atoms evolved freely in the microcanonical ensemble (NVE).

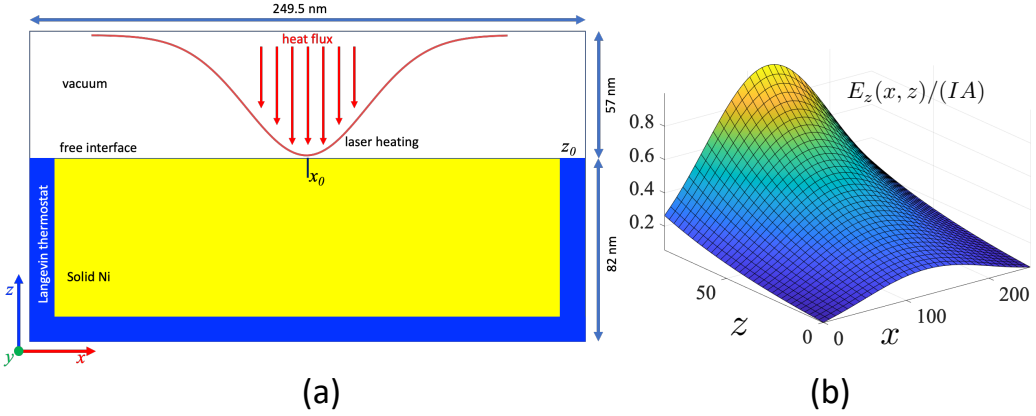

Figure 1: (a) Schematic representation of the simulation box. In the border zones in blue, the Ni atoms are thermalized at 1300 K with a Langevin thermostat. Other atoms colored in yellow evolve freely in the microcanonical ensemble. (b) Function E_z given by (2).

Continuous local heating of the surface, mimicking the effect of a laser beam, was performed by adding non-translational kinetic energy (heat) to atoms. Laser heating is

modeled by a Gaussian energy flux (eV ps^{-1}), which is given by:

$$E_z = IA \exp\left(-\frac{(x-x_0)^2}{2\sigma_r^2}\right) \exp\left(-\frac{|z-z_0|}{\lambda}\right) \tag{2}$$

where I is the laser intensity (eV Å^{-2}ps^{-1}), A is the surface beam area (Å^2), x_0 is the center of the laser beam, z_0 is the surface position, and λ is the absorption (optical) depth. The variance σ_r is related to the full width at half maximum r_g: $2\sqrt{2\ln 2}\sigma_r \equiv r_g$. The right term in (2) describes the absorption of laser radiation in a metallic system, at a given depth z, and follows the Beer-Lambert law. In the simulations, we chose $r_g = 1800$ Å and $\lambda = 525$ Å. The optical depth was deliberately selected to counter-balance the artificial low thermal conductivity of Ni as calculated by the potential. This adjustment enabled us to achieve a melt pool geometry closely resembling that observed in experiments. In real systems, the optical depth is ranging from 100 to 200 Å, as a function of the laser wavelength.

Fast melting of the nickel below the beam was achieved by applying a laser intensity of $I = 3 \times 10^{-4}$ eV Å^{-2}ps^{-1} during 0.3 ns. This heating procedure allowed an average temperature of $\sim$1950 K (i.e., above 1701 K, the melting temperature of Nickel with the potential) below the incident beam to be reached rapidly. The melt pool was then slowly and continuously heated (i.e., 0.58 K ps^{-1}) with a laser intensity of $I = 4 \times 10^{-5}$ eV Å^{-2}ps^{-1}. Different laser intensities ranging from $I = 2 \times 10^{-5}$ to 5×10^{-5} eV Å^{-2}ps^{-1} were also considered. System visualization and thermal analysis were performed with OVITO software [30]

III. RESULTS

A. Hydrodynamics of liquid nickel

The ability of MD simulations to describe a physical system relies on the accuracy of the interatomic potential and model design. Once the interatomic potential is defined,

MD simulations are carried out without any further parameter adjustment. This technique, thus, provides a useful tool for investigating physical processes at nanoscale. In this context, it is interesting to evaluate the system properties that govern the hydrodynamics of liquid nickel (see Table I). The MD model (Sec. II) captures the key aspects of a laser surface treatment: the solid surface is heated by a localized Gaussian heat flux and a melt pool is created. Heat transfer is directly related to conduction and convection (radiation is neglected). If a fluid flow is observed in the melt, it is only associated with thermocapillary convection. Since the driving force for melt pool movement is surface tension, we first estimated the temperature dependence of surface tension of a free surface in the case of liquid nickel.

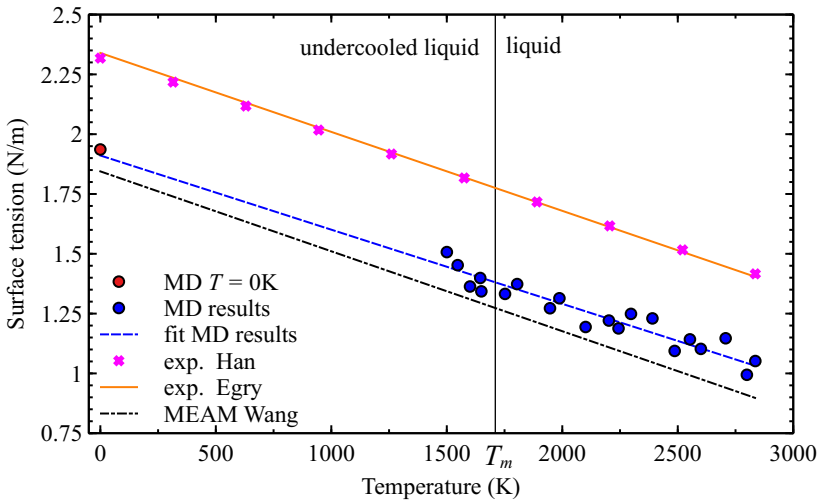

Figure 2: Surface tension as a function of temperature: MD results compared to existing experimental data. Experimental values reported in the literature are as follows: $\gamma = 1.769 - 3.18 \times 10^{-4}(T - T_m)$ in Han *et al.* [33] and $\gamma = 1.770 - 3.30 \times 10^{-4}(T - T_m)$ in Egry *et al.* [34]. Note that MD results using MEAM potential [35] are also plotted.

We considered a two-phase system with its liquid-vapor interface oriented perpendicularly to the z direction at different temperatures above the melting point (liquid) and

below this point (undercooled liquid) [31]. The surface tension is given in terms of the pressure [32]:

$$\gamma = \frac{L_z}{2}\left(\langle P_{zz}\rangle - \frac{\langle P_{xx}\rangle + \langle P_{yy}\rangle}{2}\right) \tag{3}$$

where L_z is the length of the simulation cell in the direction perpendicular to the interface and $P_{aa}\,(a = x, y, z)$ denotes the diagonal component of the pressure tensor. The brackets $\langle\rangle$ refer to the time average.

Figure 2 depicts the temperature dependence of surface tension. Simulation results using eq. (3) are compared to experimental values. The fit of simulation results demonstrates a linear dependence as predicted by eq. (1). Surface tension values measured in MD are slightly lower than experimental values (10%), but the linear regression coefficient γ_T is very close to the experimental one. Values reported in Ref. [35], using a MEAM potential for the liquid metal, are also lower than experimental ones .

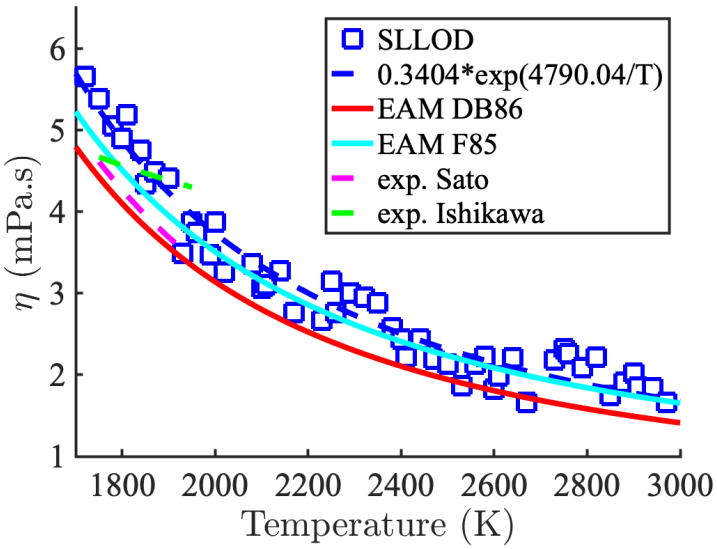

Figure 3: Viscosity as a function of temperature. The present MD results obtained with the SLLOD method are compared to the experimental data (i.e. Sato [37] and Ishikawa [38]) and to numerical simulations (i.e. F85 = [39] and DB86 =[40]) compiled in Rozas et al. [41].

In order to estimate the viscous forces, we calculated the viscosity of liquid Ni using the SLLOD method [36]. Calculated viscosity and experimental value are of the same order of magnitude. A fit of the present MD results gives the temperature dependence : $\eta = 0.3404 \exp(4790/T) \times 10^{-3}$ kg m^{-1} s^{-1} (Fig. 3).

The thermal conductivity that governs heat conduction has been estimated in Ref. [42]. The huge discrepancy between the experimental and MD data for heat conductivity can easily be understood if one considers that the conduction of heat observed in this MD study with the classical potential accounts only for phonon transport and does not account for electronic transport. In the case of our Ni system, the MD value led to an effective characteristic length of heat conduction that was shorter than the real one by a factor $\mathscr{L}_{\text{exp}}/\mathscr{L}_{\text{MD}} = 4.2$. This can be considered an asset in simulations because we can investigate thermal effects at MD scales.

Table I summarizes the main parameters that control the fluid flow in the case of thermocapillary convection. The thermodynamic and physical properties of Ni calculated by MD using the EAM potential [28] are compared to experimental values or thermodynamic estimations. Temperature-dependent parameters are evaluated at the bulk melting temperature T_m.

In the present system, the melt pool is subjected to heat transfer, viscosity, and surface tension. We first estimated the typical time scales associated with the characteristic transport phenomena. A thermal fluctuation of length scale ℓ will be damped by heat transfer after time ℓ^2/κ, where κ is the thermal diffusivity (m^{2}s^{-1}). The longest thermal time scale is associated with thermal fluctuations over the entire system of size d,

$$\tau_{\text{th}} = d^2/\kappa \tag{4}$$

Velocity fluctuations decay after a time corresponding to the viscous time scale

$$\tau_{\text{vis}} = d^2/\nu \tag{5}$$

where ν is the viscosity (m^{2}s^{-1}). The Prandtl number, Pr, measures the ratio between

parameter	symbol	MD	Exp
bulk melting temperature	T_m	1701 K	1727 K [a]
density (liquid)	$\rho = M/V_m(\text{liq})$	7.966×10^3 kg m^{-3}	7.93×10^3 kg m^{-3} [a]
heat conductivity	λ	2.8 W m^{-1} K^{-1}	54.182 W m^{-1} K^{-1} [b]
heat capacity	C_p	655 J kg^{-1} K^{-1}	680 J kg^{-1} K^{-1} [c]
heat diffusivity	$\kappa = \lambda/\rho C_p$	5.37×10^{-7} m^2 s^{-1}	100×10^{-7} m^2 s^{-1}
kinematic viscosity	η	5.68×10^{-3} kg m^{-1} s^{-1}	$4.5 - 6 \times 10^{-3}$ kg m^{-1} s^{-1}
viscosity	$\nu = \eta/\rho$	7.13×10^{-7} m^{2}s^{-1}	7.68×10^{-7} m^2 s^{-1}
surface tension at T_m	γ_m	1.381 N m^{-1} (kg s^{-2})	1.769 N m^{-1} [e]
surface tension coefficient	γ_T	3.1×10^{-4} kg s^{-2} K^{-1}	3.18×10^{-4} kg s^{-2} K^{-1} [e]
Prandtl number	$Pr = \kappa/\nu$	1.32	7.68×10^{-2}
Marangoni prefactor	$\gamma_T/(\kappa \times \eta)$	1.017×10^5 m^{-1} K^{-1}	5.3×10^3 m^{-1} K^{-1}

Table I: Parameters of pure Ni computed with the EAM interatomic potential [28, 29, 42] and compared to experimental values or thermodynamic calculations ([a] Brillo and Egry[43] ; [b] Assael *et al.* [44]; [c] Ishikawa *et al.* [45] [d] Thermo-Calc ®[e] Han [33]). Temperature-dependent parameters are evaluated at the bulk melting temperature T_m.

viscous and thermal effects,

$$Pr = \frac{\nu}{\kappa} = \frac{\tau_{\text{th}}}{\tau_{\text{vis}}} \tag{6}$$

which is very small for liquid metals ($10^{-2} - 10^{-3}$, 7.68×10^{-2} for liquid nickel at melting point). The low value of Pr means that thermal relaxation is much faster than viscous effects. In MD simulations (see Table I), thermal and viscous time scales are of the same order of magnitude.

When a thermal gradient $\beta = \Delta T/d$ is applied along the interface of a fluid of density ρ, the stress due to surface tension gradient, $\nabla\gamma = \gamma_T\beta$, acts tangentially, and the fluid experiences an acceleration $\gamma_T\beta/\rho d$. The characteristic time associated with surface

stress reads

$$\tau_{\mathrm{Ma}} = \left(\frac{\rho d^2}{\gamma_T \beta}\right)^{-1/2} \tag{7}$$

The Marangoni number measures the ratio between dissipative processes and surface tension effects (advective and diffusive transport),

$$\mathrm{Ma} = \frac{\tau_{\mathrm{th}}\tau_{\mathrm{vis}}}{\tau_{\mathrm{Ma}}^2} = \frac{\gamma_T \Delta T\, d}{\kappa \eta} \tag{8}$$

where $\eta = \rho\nu$ is the kinematic viscosity (kg $\mathrm{m}^{-1}\mathrm{s}^{-1}$). The Marangoni prefactor, $\gamma_T/\kappa\eta$, estimated in MD is much larger than the experimental value (see Table I). However, because the melt pool size is nanometric in comparison to typical micrometric melt pools observed in welding, the Marangoni number in MD could be of the same order of magnitude as in welding experiments. From the similarity law of hydrodynamics, the fluid flow observed in MD can be expected to resemble that observed in real experiments.

In the present study, we did not consider the influence of gravity and, consequently, disregarded buoyancy effects. Previous studies in welding demonstrated that buoyancy forces are generally very small in relation to other forces in weld pools of less than 10 mm depth [46].

Another approach to gauge the significance of buoyancy is by evaluating the Rayleigh number, which accounts for thermo-gravitational effects [47],

$$\mathrm{Ra} = \frac{g\,\alpha\,\Delta T\,h^3}{\kappa\,\nu} \tag{9}$$

where g is the gravitational acceleration, α is the thermal expansion coefficient, ΔT is the temperature difference, h is the thickness of the layer, κ is the thermal diffusivity, and ν is the viscosity. Considering the values provided in Table I with h set at 50 nm and α at $10^{-5}\,\mathrm{K}^{-1}$ [48], the computed Rayleigh number for the simulated system is found to be

$$\mathrm{Ra} = 1.2 \times 10^{-10}. \tag{10}$$

This estimation confirms the marginal impact of gravitational effects in our simulations.

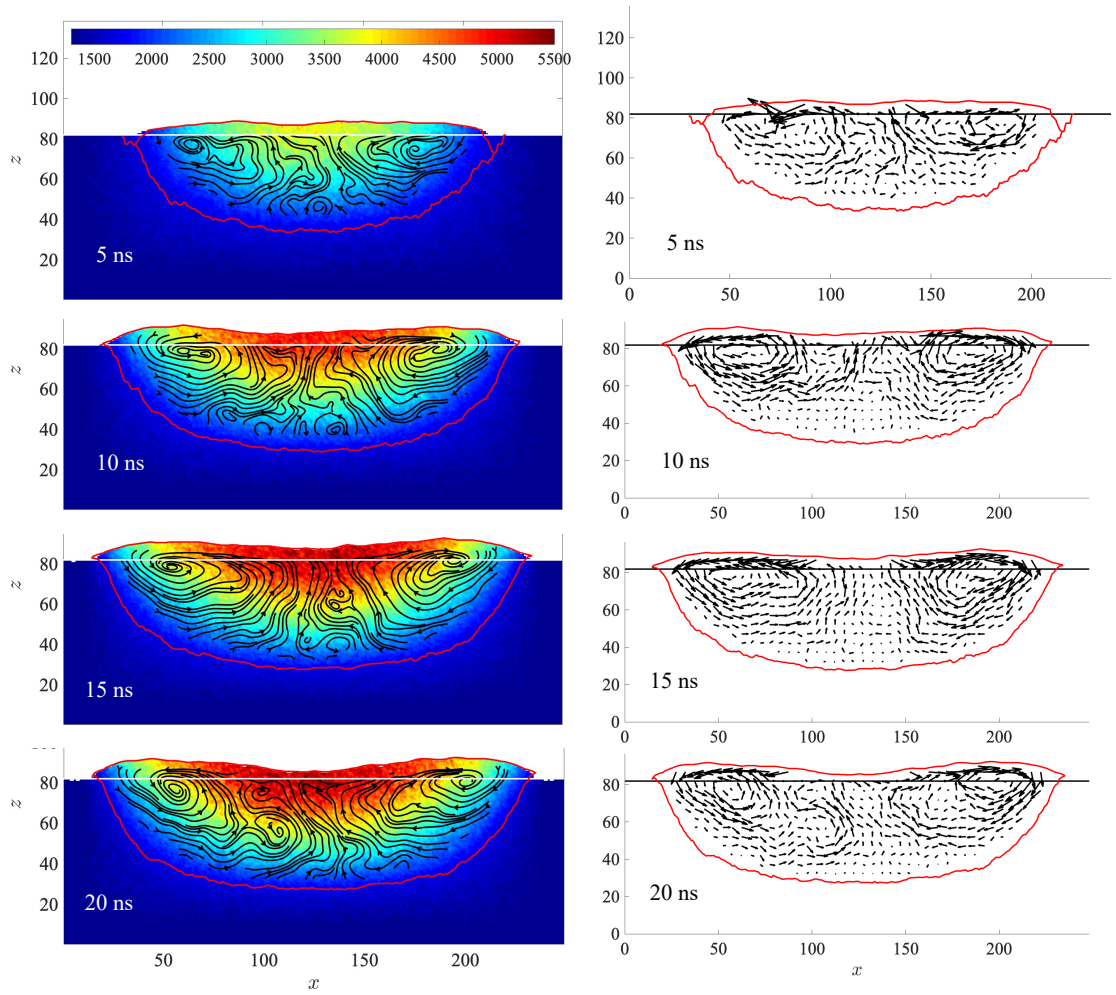

Figure 4: Snapshots of the system at different times with $I = 4 \times 10^{-5}$ eV Å^{-2} ps^{-1}. Units of x and z axes are in nm. Left: Temperature distribution (K) and streamlines. The colorbar gives the temperature range between 1100 K and 5500 K. The sample was divided into 250 $\times$ 140 bins. The temperature in each bin was obtained by averaging the temperature of the atoms belonging to the considered bin. Right: Displacement vectors (in nm) computed by subtracting the atomic coordinates at $t - 0.5$ ns from those at t ns. The red curve delineates the melt pool.

B. Study of melt pool dynamics

We first studied melt pool formation during laser heating, with the establishment of a stationary temperature gradient, and the movement of atoms in a representative case with $I = 4 \times 10^{-5}$ eV Å^{-2} ps^{-1} (Fig. 4):

- The Gaussian laser beam induced the formation of a concave melt pool in the solid part. Because of thermal expansion, liquid Ni expanded at the liquid/vacuum interface. After a transient stage, the melt pool exhibited a non-flat shape with extra liquid at its edges.

- The continuous laser heating combined with cooling by conduction in the solid part gave rise to a radial temperature gradient. The maximum temperature was located at the center of the laser beam (x_0, z_0) (see Fig. 1).

- As the temperature gradient increased, the fluid started to move, with the appearance of a flow structure. The liquid at the center of the pool surface flowed outward along the pool surface, turned downward at the pool edge, and returned to the center. Two counter-rotating cells were observed.

At the surface, localized heating induced a temperature gradient, $\beta = \nabla T = dT/dx$, from the center of the melt pool to its edges. As a consequence (eq. (1), Fig. 2), this induced a "reverse" surface tension gradient and a tangential constraint $\sigma = -|\gamma_T|\,\gamma_m \nabla T$ along the interface. The fluid was pulled along the surface from the center, where the temperature is high and the surface tension is low, to the edges, where the temperature is low and the surface tension is high. Figure 5a depicts the "surface" velocity u in the x direction, together with the temperature profile along the interface. These quantities were averaged in a slice δ_v on both sides of the interface ($z = 82$ nm). We observed the establishment of a temperature gradient between the center (x_0, z_0), where the laser intensity is maximum, and the edge of the melt pool, corresponding to T_m. The temperature further decreased in the solid because of the thermostated layers. The velocity (absolute

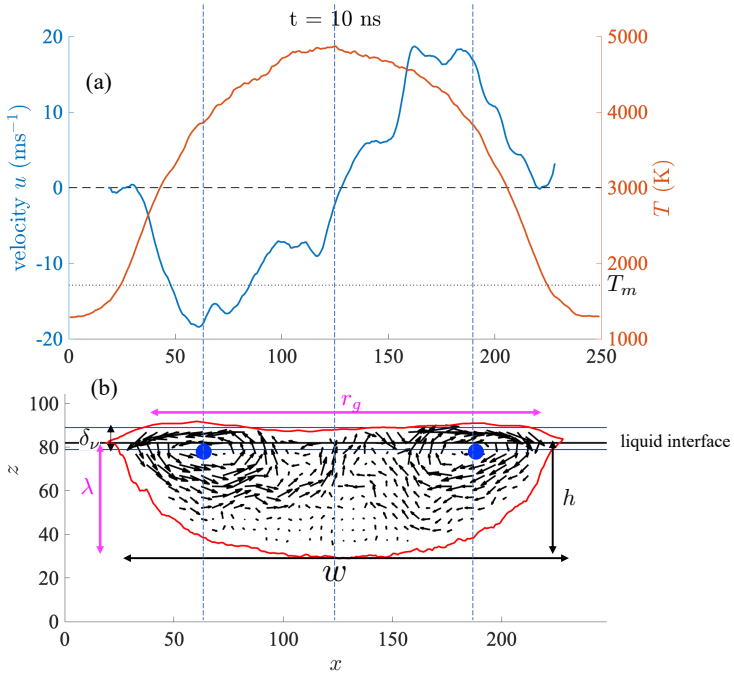

Figure 5: Analysis of the system of Fig. 4. (a): Flow velocity, u, in the x direction and temperature profile, T, as a function of x at this interface. Temperature is evaluated in the upper layer of width δ_v (b): Displacement vectors (in nm); w and h are the melt pool width and depth; λ is the characteristic absorption depth of the laser beam (eq. 2) and r_g is the full width at half maximum. The red curve delineates the melt pool (solid-liquid and liquid-gas boundaries). The black line indicates the liquid interface when aligned with the solid-gas interface. The blue lines correspond to the limits of the viscous slice of depth δ_v. Blue dots correspond to the convection cell centers. Units of x and z axes are in nm.

value) in the boundary layer increased, reaching a maximum before decreasing sharply at pool edges. The atom displacements at $t = 10$ ns in the xz plane are displayed in Fig. 5b. Displacements were computed by subtracting the atomic coordinates at 9.5 ns from those at 10 ns. The flow is relatively fast along the free surface (surface flow) and weaker in the pool (return flow). The cell centers are near the pool surface and close to the edge. Fluid at the bottom of the pool is almost at rest. This flow is characteristic of

thermocapillary convection [13].

The melt pool has a typical concave shape. Its width w slightly exceeds the full width at half maximum (FWHM) of the laser beam r_g; its extent could be greater if the system was not confined by thermalized walls. Its depth h corresponds to the laser absorption depth λ. At the top, the melt pool exhibits a convex shape where the flow velocity is maximum.

When the fluid started to move because of surface tension variations, the fluid experienced a viscous shear stress. Thermocapillary forces responsible for the outward fluid flow are balanced by viscous stress along the free surface. In other words, the global constraint must vanish at the free interface:

$$-\eta \left(\frac{\partial u}{\partial z}\right)_{\text{sfc}} - |\gamma_T|\beta = 0 \tag{11}$$

where u is the velocity in the x direction. The velocity v in the z direction is assumed to be equal to zero.

Equation (11) is often used in the scaling analysis [49]: U represents the surface flow velocity, δ_v is the shear layer beneath the free surface, and w is the characteristic melt pool width. If we take $\delta_v = 10$ nm, $w/2 = 100$ nm, we obtain the rough estimation

$$U = \frac{\gamma_T \Delta T}{\eta} \frac{\delta_v}{w/2} \sim 18\,\text{m/s} \tag{12}$$

close to the measured velocity. The system, which is continuously irradiated by an incident flux, is in contact with thermalized walls. Figure 6a shows the instantaneous temperature profile calculated in the upper layer, of width δ_v, close to the interface, at different times. The temperature profile has a bell-shaped curve, decreasing from its maximum to wall temperature, precisely mirroring laser intensity (eq. (2)). The temperature profile progressively reached a steady profile, with a maximum around 5200 K. The width of the pool, delineated by the melting temperature, increased to $w_{\text{max}} \approx 213$ nm. The velocity in the x direction in the viscous layer, u_δ, is depicted in Fig. 6b. The profile is symmetrical around the system center (x = 125 nm), reflecting the two

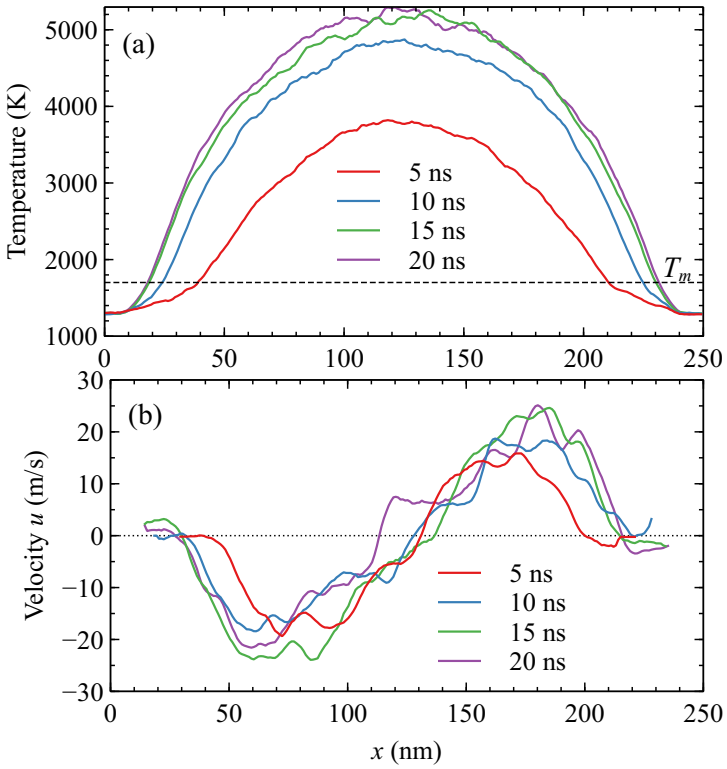

Figure 6: (a) Instantaneous temperature profiles, in the x direction, at different times. Temperature is evaluated in the upper layer of width δ_v, close to the interface. (b) Flow velocity u_δ at different times. The laser intensity is $I = 4 \times 10^{-5}$ eV Å^{-2} ps^{-1}.

counter-rotating eddies. The fact that u_δ is close to zero in the melt pool center corresponds to the upward flow. The peak velocity increased from 16 to 25 m/s during the transient stage before the stationary state and shifted to the right (left), close to the pool edges and just in front of the cell centers. The velocity decreased abruptly from its maximum to zero because the flow followed the melt pool curve. At 20 ns, u_δ was no longer strictly symmetrical (it crossed zero at 110 nm), reflecting a left convection cell splitting into two eddies (see Fig. 4).

Influence of laser intensity

We investigated the effect of the energy deposited by the laser on system behavior,

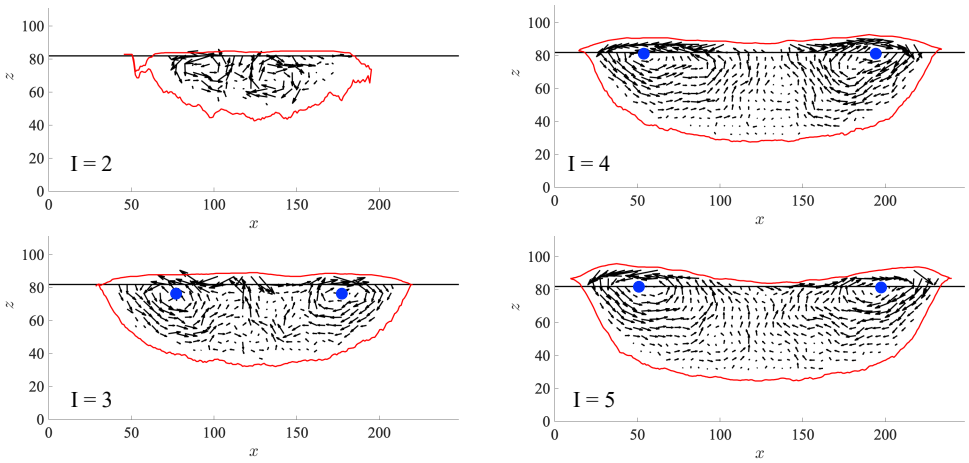

Figure 7: Flow field when varying laser intensity I ($\times$ 10^{-5} eV Å^{-2} ps^{-1}), at 15 ns. Displacement vectors (in nm) were computed by subtracting the atomic coordinates at $t-0.5$ ns from those at t ns. The red curve delineates the melt pool (solid-liquid and liquid-gas boundaries). The black line indicates the liquid interface when aligned with the solid-gas interface. Units of x and z axes are in nm.

with laser intensity I in the range $2-5\times10^{-5}$ eV Å^{-2} ps^{-1}. For this purpose, we compared systems once they have reached a stationary state with well-established convection rolls; $t=15$ ns seemed an appropriate choice (see Fig. 7). In what follows, we will not repeat the units for I, for the sake of convenience. In the case $I=2\times10^{-5}$, fluid motion was erratic. A collective movement was observable for $I=3\times10^{-5}$. For higher laser intensities, the flow self-organized into convective cells.

The first step was to characterize the shape of the melt pool. Its depth h was measured as the difference between the solid/gas interface and the pool bottom. Its width w was defined as the difference between the solid-liquid limits at the solid-gas interface. As shown in Fig. 8a, the depth depends weakly on I because the depth mainly depends on the laser absorption depth, λ. The pool width increased with I, up to $I=4\times10^{-5}$, and then saturated. This is related to the finite system size: the pool edges were closer

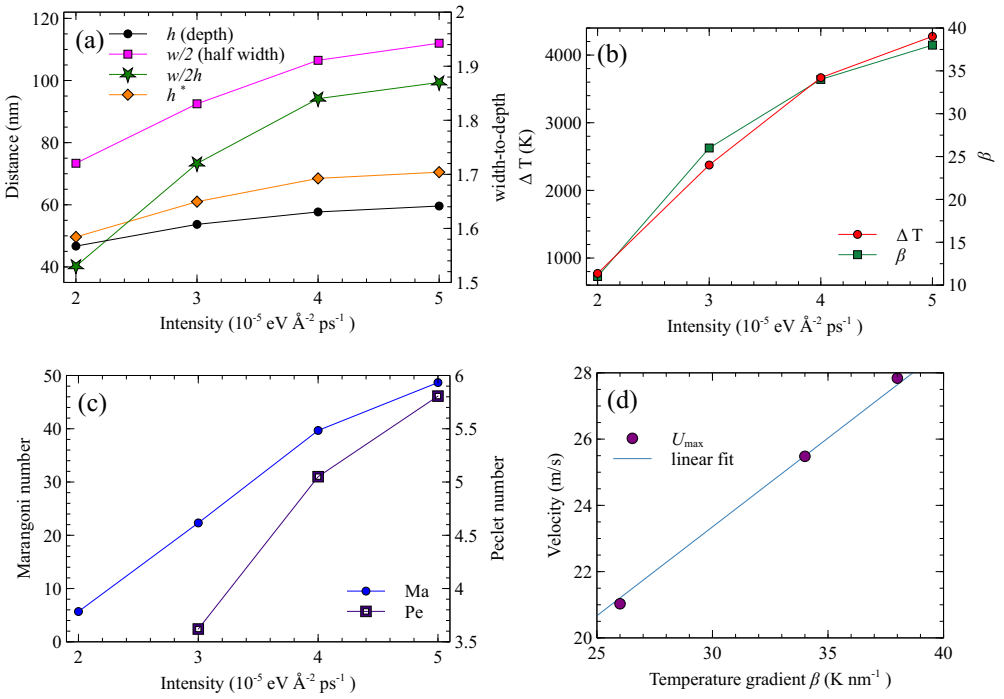

Figure 8: Influence of laser intensity I (a) Melt pool characteristics: depths h and h^* (see text), and half-width $w/2$ (left), width-to-depth ratio (right) (b) Temperature difference between pool center and edges (left) and temperature gradient (right) (c) Marangoni number (left) and Péclet number (right) (d) Maximum velocity U measured as a function of temperature gradient. All quantities were estimated at 15 ns.

to the thermal walls (Fig. 8a). The finite system size also induced a modification of the shape of the liquid-gas interface. For low I values, the shape was convex, reflecting the expansion of the liquid at high temperatures. For higher I values, the interface shape became curved, with a central concavity (see Fig. 7). This observation is corroborated by the measurement of the maximum liquid thickness h^*. The difference $h^* - h$ corresponds to the maximum thickness of the liquid above the solid, increasing with I. There was a rise of liquid along the edges. As measured by the width-to-depth ratio, the pool

shape was not semi-spherical ($w/2h = 1$) but semi-ellipsoidal, with $w/2h > 1$. The melt pool elongated with increasing I.

The temperature difference ΔT is plotted in Fig. 8b; ΔT is the difference between the maximum temperature located at the pool center and the melting temperature T_m at the pool edges. This value increased with laser intensity but saturated for $I = 5 \times 10^{-5}$. This is due to the fact that heat is evacuated more efficiently when melt pool edges are closer to thermostated walls.

The Marangoni number (eq. (8)) was evaluated using the parameters in Table I and measured values of half pool width $w/2$ and temperature gradient β. As shown in Fig. 8c, the Marangoni number increased as a function of laser intensity I. This result reflects the increase in temperature ΔT and in pool width for more powerful lasers. These values are in a typical range that has been reported for real systems (Ma < 100). In our case, we can vary Ma by changing the laser power, but Pr remains fixed because it is a material property. For these typical values, the melt pool shape is expected to be concave (hemispherical) as predicted numerically in Ref. [50], in agreement with our MD observations.

The maximum velocity in the viscous layer at the liquid/gas interface, $U_{\max}$, was evaluated for $I = 3 \times 10^{-5}$, 4×10^{-5} and 5×10^{-5}. Figure 7d depicts $U_{\max}$ as a function of temperature gradient, β, and the linear fit is $a\beta + b$, where $a = 0.536$. The coefficient a was compared to the coefficient in eq. (12): $\gamma_T \delta_v / \eta$ = 0.546 (with $\delta_v = 10$ nm). This demonstrates that eq. (12) provides a reasonable estimation of the maximum velocity in the viscous layer.

One way to characterize the contribution of heat transfer by conduction and by convection is provided by the Péclet number. The Péclet number is defined by the product of maximum surface speed U and the radius of the pool divided by thermal diffusivity, indicating the relative importance of heat transport by convection in comparison with heat transport by conduction.

$$\mathrm{Pe} = \frac{\tau_{\mathrm{th-cond}}}{\tau_{\mathrm{th-conv}}} = \frac{Ud}{\kappa} \tag{13}$$

with $d = w/2$. The Péclet number is not a material constant, as it depends both on the velocity of the flow field and on a characteristic length of the system. In our case, Pe > 1 and $\tau_{\mathrm{th-cond}} > \tau_{\mathrm{th-conv}}$. In other words, convection is more efficient than conduction for heat transport.

Influence of system size

parameter		system A (small)	system B (large)
System size	L_x (nm)	250	357
	L_z (nm)	139	175
Melt pool characteristics	Depth h (nm)	58	71
	Half width $w/2$ (nm)	107	119
	Width-to-depth $w/2$	1.85	1.66
Temperature difference	ΔT (K)	3666	2058
Temperature gradient	β (K nm^{-1})	34.26	17.29
Maximum speed	$u_\delta^{\max}$ (m/s)	25.5	12.6
Marangoni number	Ma	40	25
Péclet number	Pe	5.05	2.09

Table II: Comparison between small (A) and large (B) systems, at $t = 20$ ns with $I = 4 \times 10^{-5}$.

We also investigated the influence of the laser beam diameter. In order to mimic this situation in MD, we considered a large system in a simulation box of size L_x = 357 nm $\times$ L_y = 1.4 nm $\times$ L_y = 175 nm. The large system is called B and the reference system (described in Sec. II) is called A. The size of thermalized walls was the same as in the reference system. Parameters and physical quantities are reported in Table II. We compared both systems at $t = 20$ ns and $I = 4 \times 10^{-5}$. The characteristic length of thermal diffusion corresponding to 20 ns is $d_{\mathrm{th}} = 104$ nm (eq. (4)). The melt pool of system B was larger in width and depth but its width-to-depth is smaller than that of

system A. This corresponds to a less elongated shape. Its width (238 nm) exceeded the full width at half maximum of the laser beam ($r_g = 180$ nm) and its depth (71 nm) was larger than the absorption length of the laser (52.5 nm).

The most striking observation is the drastic reduction in the temperature at the center of the melt pool. This is due to the fact that the heat delivered by the laser is transported by conduction away from the center both in the melt pool and in the solid part. The gradient is half as large in the large system. The maximum velocity in the boundary layer, $u_\delta^{\max}$, is reduced by a factor of 2 in system B compared to system A. The Péclet number is also smaller in system B than in system A. This corresponds to a situation where the heat transport by convection is less efficient.

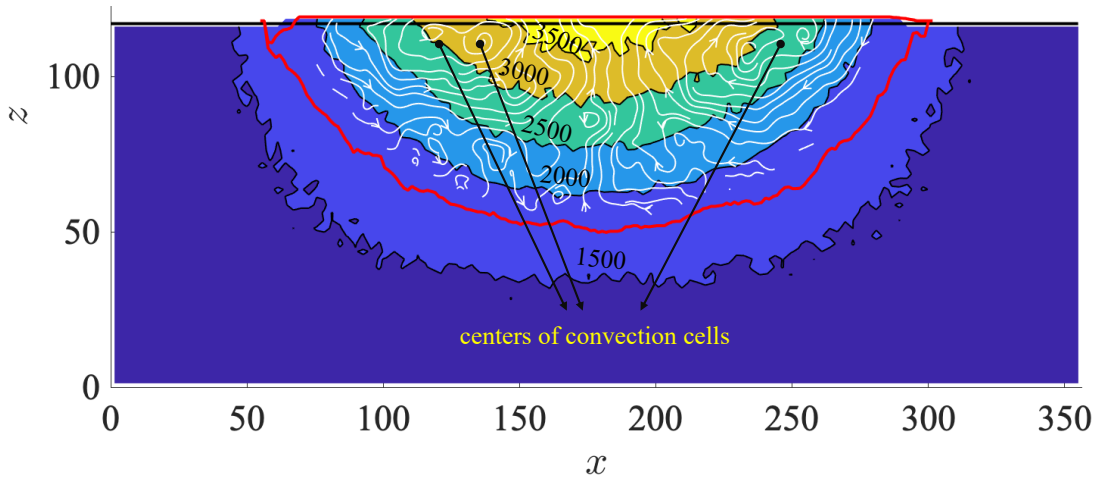

Figure 9: Snapshot of system B at $t = 20$ ns. Temperature distribution (K) and streamlines (in white). The sample was divided into 250 $\times$ 140 bins. The temperature in each bin was obtained by averaging the temperature of the atoms belonging to the considered bin. The red curve delineates the melt pool.

Figure 9 shows the flow pattern together with temperature distribution. The interface is relatively flat and the expansion of the liquid is limited. The convection cell centers are located farther from the edges than in system A. The fluid flow is steady and es-

sentially unicellular. Nevertheless, we note a double center in the left convection cell and weaker secondary cells near the pool bottom. Limmaneevichitr and Kou studied the effect of the diameter and power of the laser beam in Ref. [13]. They reported that convection is deeper and slower for a lower laser beam power or a larger beam diameter. In other words, the large system, B, corresponds to situations where the power of the laser beam is lower or where the laser beam diameter is larger.

IV. CONCLUSIONS

In the present work, we studied a situation in which a focused heat source applied on the free surface of a Ni block created a melt pool. Because of the variations in surface tension along the gas/liquid interface, the liquid metal flowed toward the pool edges, in the direction of high surface tension. The slope of the surface tension gradient is the opposite of the temperature gradient slope. This outward fluid motion induced the formation of convection cells with upward flow in the melt pool center.

In other words, thermocapillary convection was evidenced at the nanoscale. By means of MD simulations, we were able to isolate thermal effects and demonstrate that surface tension gradient is the driving force in this phenomenon. The model designed in MD is very similar to the device used in experimental setup to study weld pools [13]; however, strictly speaking, only low-gravity experiments are able to isolate purely thermal effects. In addition,molecular dynamics is an approach in which all thermal and transport properties are fixed by the choice of the interatomic potential. We, thus, calculated the temperature dependence of surface tension and viscosity of pure liquid Ni. This systematic evaluation of physical properties allowed us to classify the observations according to non-dimensional numbers, linking the nanoscale flow to fluid dynamics.

The parameter values used in the simulation appear unrealistic at first sight. For instance, the full width at half maximum of the heat source must be small relative to the system size. This nanometric value (180 nm) was, thus, compensated by a huge laser

intensity value in order to provide a sufficient amount of heat. The same type of scaling applies to non-dimensional numbers governing the hydrodynamic behavior. Indeed, the Marangoni number is in the range of [10 - 100], and the Prandtl number is close to unity. For these particular values, the analysis based on CFD predicts a behavior similar to the one observed in MD simulations [49] .

The main results of MD simulations are as follows:

- The melt pool is a half ellipse drawn by the Gaussian heat source.
- The temperature gradient at the surface induces a surface tension gradient that is the driving force for the nanoscale flow.
- Fluid flow patterns developed in the form of two typical counter-rotating convection cells.
- Fluid flow characteristics depend on laser beam power and system geometry.
- Both conduction and convection play a role in heat transfer.

No significant departure from what is observed in a micrometric system was noticed in MD simulations. This result is probably related to the fact that the order of magnitude of Marangoni and Prandtl numbers are similar at both scales.

Melt pool formation is a ubiquitous feature in laser material processing, including welding and additive manufacturing. The understanding of melt pool dynamics is of primary importance in the context of solidification processes, in order to control the characteristics of fabricated parts. Molecular dynamics simulations could be used to describe the solidification processes of the melt pool, at the nanoscale, following the lines of our previous work [42]. By considering a melt pool in a polycrystalline Ni system, the competition between columnar and equiaxed grains would be explored during solidification when both convection and conduction heat transfer are taken into account. Another interesting aspect is the motion of inoculants or tracers during the cooling of the melt pool and their impact on the final microstructure. In summary, MD simulations are able to capture transient behaviors associated with thermocapillary convection in

metallic systems due to laser heating and to assess their influence on the microstructure when solidification is completed.

ACKNOWLEDGMENTS

The use of computational facilities at the Computing Center of the University of Bourgogne, DNUM-CCUB, is gratefully acknowledged. The authors thank Carmela Chateau-Smith for the careful reading of the manuscript.

---

[1] Sindo Kou, *Welding Metallurgy*, John Wiley & Sons Eds., 3rd edition (2020) ISBN 0-471-43491-4

[2] G. Xie, G. Lv , Y. Wang , W. Ma , X. Yang , Y. Lei, The influence of Marangoni effect on the growth quality of multi-crystalline silicon during the vacuum directional solidification process, Mater. Sci. Semicond. Process. 91, 124-132 (2019)
doi: 10.1016/j.mssp.2018.11.015

[3] V. S. Ajaev, Instability and rupture of thin liquid films on solid substrates, Interfacial Phenom. Heat Transf., 1, 81-92 (2013)
doi: 10.1615/InterfacPhenomHeatTransfer.2013006838

[4] T. D. Bennett, D. J. Krajnovich, C. P. Grigoropoulos, P. Baumgart, A. C. Tam, Marangoni mechanism in pulsed laser texturing of magnetic disk substrates, J. Heat Transfer 119, 589-596 (1997)
doi: 10.1115/1.2824146

[5] W.H. Yu, S.L. Sing, C.K. Chua, C.N Kuo, X.L. Tian, Particle-reinforced metal matrix nanocomposites fabricated by selective laser melting: A state of the art review, Prog. Mater. Sci. 104, 330-379 (2019)
doi:10.1016/j.pmatsci.2019.04.006

[6] M. Gäumann, S. Henry, F. Cléton, J.-D. Wagnière, W. Kurz, Epitaxial laser metal forming: analysis of microstructure formation, Mater. Sci. Eng. A 271, 232-241 (1999)
doi: 10.1016/S0921-5093(99)00202-6

[7] A. Hartnett, I. Seric, K. Mahady, L. Kondic, S. Afkhami, J. D. Fowlkes, and P. D. Rack, Exploiting the Marangoni effect to initiate instabilities and direct the assembly of liquid metal filaments, Langmuir 33, 8123-8128 (2017)
doi:10.1021/acs.langmuir.7b01655

[8] D. Sharma, P. K. Ghosh, S. Kumar, S. Das, R. Anant, N. Kumar, Surface hardening by in-situ grown composite layer on microalloyed steel employing TIG arcing process, Surf. Coat. 352, 144-158 (2018)
doi: 10.1016/j.surfcoat.2018.08.009

[9] H. Bénard, Les tourbillons cellulaires dans une nappe liquide, Rev. Gén. Sci. Pures Appl. 11, 1261-1271 (1900)
doi:10.1051/jphystap:0190100100025400

[10] J.R.A. Pearson, On convection cells induced by surface tension, J. Fluid Mech. 4, 489-500 (1958)
doi: 10.1017/S0022112058000616

[11] M.F. Schatz and G.P. Neitzel, Experiments on thermocapillary instabilities, Annu. Rev. Fluid Mech. 33, 93-127 (2001)
doi: 10.1146/annurev.fluid.33.1.93

[12] A. Eyer, H. Leiste, H. Nitsche, Floating-zone growth of silicon under microgravity in a sounding rocket, J. Cryst. Growth 71, 173-182 (1985)
doi: 10.1016/0022-0248(85)90059-4

[13] C. Limmaneevichitr and S. Kou, Visualization of Marangoni convection in simulated weld pools, Welding Research Supplement 79, 126-135 (2000)

[14] H. Shen, J. Yan, X. Niu, Thermo-fluid-dynamics modeling of the melt pool during selective laser melting for AZ91D Magnesium alloy, Materials 13, 4157 (2020)

doi: 10.3390/ma13184157

[15] M. Mareschal and E. Kestemont, Experimental evidence for convective rolls in finite two-dimensional molecular models, Nature 323, 427 (1987)
doi: 10.1038/329427a0

[16] M. Mareschal, M. Malek Mansour, A. Puhl and E. Kestemont, Molecular dynamics versus hydrodynamics in a two-dimensional Rayleigh-Bénard system, Phys. Rev. Lett. 61, 2550 (1988)
doi: 10.1103/PhysRevLett.61.2550

[17] F. Baras, M. Malek Mansour, A.L. Garcia and M. Mareschal, Particle Simulation of Complex Flows in Dilute Systems, J. Comput. Phys. 119, 84-104 (1995)
doi: 10.1006/jcph.1995.1118

[18] M.A. Gallis,T.P. Koehler,J.R. Torczynski,and S.J. Plimpton, Direct simulation Monte Carlo investigation of the Rayleigh-Taylor instability, Phys. Rev. Fluids 1, 043403 (2016)
doi: 10.1103/PhysRevFluids.1.043403

[19] J. L. Barber, K. Kadau, T. C. Germann, P. S. Lomdahl, B. L. Holian and B. J. Alder, Atomistic simulation of the Rayleigh-Taylor instability, J. Phys. Conf. Ser. 46, 58-62 (2006)
doi: 10.1088/1742-6596/46/1/008

[20] C. Zhao, J.E. Sprittles and D.A. Lockerby, Revisting the Raileigh-Plateau instability for the nanoscale, J. Fluid Mech. 861, R3-1 (2019) doi: 10.1017/jfm.2018.950

[21] Y. Imai, T. Yamamoto, A. Sekimoto, Y. Okano, R. Sato, Y. Shigeta, Numerical investigation of the nano-scale solutal Marangoni connvections, J. Taiwan Inst. Chem. Eng. 98, 20-26 (2019)
doi:10.1016/j.jtice.2018.05.015

[22] H.A. Maier, P.A. Bopp and M.J. Hampe, Non-equilibrium molecular dynamics simulation of the thermocapillary effect, Can. J. Chem. Eng. 90, 833-842 (2012)
doi : 10.1002/cjce.21659

[23] A. Kundan, J.L. Plawsky, P.C. Jr Wayner, D.F. Chao, R.J. Sicker, B.J. Motil, T. Lorik, L. Chestney, J. Eustace, J. Zoldak, Thermocapillary Phenomena and Performance Limitations of a Wickless Heat Pipe in Microgravity, Phys. Rev. Lett. 114, 146105 (2015)
doi: 10.1103/PhysRevLett.114.146105

[24] S. YD and S.C. Maroo, Origin of Surface-Driven Passive Liquid Flows, Langmuir 32, 8593-8597 (2016)
10.1021/acs.langmuir.6b02117

[25] J.R. Felts, S. Somnath, R.H. Ewoldt, W.P. King, Nanometer-scale flow of molten polyethylene from a heated atomic force microscope tip, Nanotechnology 23, 215301 (2012)
doi: 10.1088/0957-4484/23/21/215301

[26] K. Das, H.T. Johnson, J.B. Freund, Atomic-scale thermocapillary flow in focused ion beam milling, Phys Fluids 27, 052003 (2015)
doi: 10.1063/1.4919782

[27] S. Plimpton, Fast parallel algorithms for short-range molecular dynamics, J. Comput. Phys. 117, 1-19 (1995)
doi:10.1006/jcph.1995.1039

[28] G. Purja Pun, Y. Mishin, Development of an interatomic potential for the Ni-Al system, Phil. Mag. 89, 3245-3267 (2009)
doi: 10.1080/14786430903258184

[29] V. Turlo, F. Baras and O. Politano, Comparative study of embedded-atom methods applied to the reactivity in the Ni-Al system, Model. Simul. Mater. Sci. Eng. 25, 064002 (2017)
doi:10.1088/1361-651X/aa6cfa

[30] A. Stukowski, Visualization and analysis of atomistic simulation data with OVITO,Äìthe Open Visualization Tool, Modelling Simul. Mater. Sci. Eng. 18, 015012 (2010)
doi: 10.1088/0965-0393/18/1/015012

[31] J. Alejandre, D. J. Tildesley and G. A. Chapela, Molecular dynamics simulation of the orthobaric densities and surface tension of water, J. Chem. Phys. 102, 4574-4583 (1995)

doi: 10.1063/1.469505

[32] J. H. Irving and J. G. Kirkwood, The statistical mechanical theory of transport processes. IV. The equations of hydrodynamics, J. Chem. Phys. 18, 817-829 (1950) doi: 10.1063/1.1747782

[33] X. J. Han, N. Wang, and B. Wei, Thermophysical properties of undercooled liquid cobalt, Philos. Mag. Lett. 82, 451 (2002) doi: 10.1080/09500830210144382

[34] I. Egry, G. Lohoefer and G. Jacobs, Surface Tension of Liquid Metals: Results from Measurements on Ground and in Space, Phys. Rev. Lett. 75, 4043 (1995) doi: 10.1103/PhysRevLett.75.4043

[35] H.P. Wang, J. Chang and B. Wei, Measurement and calculation of surface tension for undercooled liquid nickel and its alloy, J. App. Phys. 106, 033506 (2009) doi: 10.1063/1.3187793

[36] Denis J. Evans and G. P. Morriss, Nonlinear-response theory for steady planar Couette flow, Phys. Rev. A 30, 1528-1530 (1984) doi: 10.1103/PhysRevA.30.1528

[37] Y. Sato, K. Sugisawa, D. Aoki, and T. Yamamura, Viscosities of Fe-Ni, Fe-Co and Ni-Co binary melts, Meas. Sci. Technol. 16, 363 (2005) doi: 10.1088/0957-0233/16/2/006

[38] T. Ishikawa, P.-F. Paradis, J. T. Okada, and Y. Watanabe, Viscosity measurements of molten refractory metals using an electrostatic levitator, Meas. Sci. Technol. 23, 025305 (2012) doi:10.1088/0957-0233/23/2/025305

[39] S. M. Foiles, Application of the embedded-atom method to liquid transition metals, Phys. Rev. B 32, 3409 (1985) doi: 10.1103/PhysRevB.32.3409

[40] S. M. Foiles, M. I. Baskes, and M. S. Daw, Embedded-atom-method functions for the fcc metals Cu, Ag, Au, Ni, Pd, Pt, and their alloys, Phys. Rev. B 33, 7983 (1986) doi: 10.1103/PhysRevB.33.7983

[41] R. E. Rozas, A. D. Demirag, P. G. Toledo and J. Horbach, Thermophysical properties of liquid Ni around the melting temperature from molecular dynamics simulation, J. Chem. Phys. 145, 064515 (2016)
doi: 10.1063/1.4960771

[42] Q. Bizot, O. Politano, V. Turlo and F. Baras, Molecular dynamics simulations of nanoscale solidification in the context of Ni additive manufacturing, Materialia 27, 101639 (2023)
doi: 10.1016/j.mtla.2022.101639

[43] J. Brillo and I. Egry, Density determination of liquid copper, nickel, and their alloys, Int. J. Thermophys. 24, 1155-1160 (2003)
doi: 10.1023/A:1025021521945

[44] M.J. Assael, A. Chatzimichailidis, K.D. Antoniadis, W.A. Wakeham, M.C. Huber and H. Fukuyamas, Reference correlations for the thermal conductivity of liquid copper, gallium, indium, iron, lead, nickel and tin, High Temp. High Press. 46, 391-416 (2017)

[45] T. Ishikawa, J.T. Okada, P.-F. Paradis, Y. Watanabe, Spectral emissivity and constant pressure heat capacity of molten nickel and rhodium measured by spectrometers combined with an electrostatic levitator, J. Chem. Thermodynamics 103, 107-114 (2016)
doi: 10.1016/j.jct.2016.08.012

[46] K.C. Mills, B.J. Keene, R.F. Brooks and A. Shirali, Marangoni effects in welding, Phil. Trans. R. Soc. Lond. A 356 911-925 (1998)
doi: 10.1098/rsta.1998.0196

[47] D. Villers and J.K. Platten, Coupled buoyancy and Marangoni convection in acetone : experiments and comparison with numerical simulations, J. Fluid Mech. 234, 487-510 (1992)
doi: 10.1017/S0022112092000880

[48] F. Baras, O. Politano, Y. Li and V. Turlo, A Molecular Dynamics study of Ag-Ni nanometric multilayers: thermal behavior and stability, Nanomaterials 13, 2134-24 (2023)
doi: 10.3390/nano13142134

[49] P.S. Wei, H.J. Liu and C.L. Lin, Scaling weld or melt pool shape induced by thermocapillary convection, Int. J. Heat Mass Transf. 55, 2328-2337 (2012)
doi: 10.1016/j.ijheatmasstransfer.2012.01.034

[50] P.S. Wei, H.J. Liu and C.L. Lin, The effects of Prandtl number on wavy weld boundary, Int. J. Heat Mass Transf. 52, 3790-3798 (2009)
doi: 10.1016/j.ijheatmasstransfer.2009.02.020